Intermetallics 18 (2010) 493–498

Contents lists available at ScienceDirect

Intermetallics

journal homepage: www.elsevier.com/locate/intermet

Cavity nucleation and growth in Cu–Zn–Al irradiated with Cu^+ ions at different temperatures

E. Zelaya [a,b,*], D. Schryvers [a], A. Tolley [b,c], P.F.P. Fitchner [d]

[a] EMAT, University of Antwerp, Groenenborgerlaan 171, B-2020 Antwerp, Belgium
[b] Consejo Nacional de Investigaciones Cientificas y Tecnicas, Argentina
[c] Centro Atómico Bariloche, Comisión Nacional de Energía Atómica, 8400 San Carlos de Bariloche, Argentina
[d] Instituto de Física, Universidade Federal do Río Grande do Sul, Porto Alegre 90035-190, RS Brasil

ARTICLE INFO

Article history:
Received 18 June 2009
Received in revised form
18 September 2009
Accepted 18 September 2009
Available online 16 October 2009

Keywords:
B. Irradiation effects
D. Defects: constitutional vacancies
F. Electron microscopy, transmission

ABSTRACT

The effects of high dose ion irradiation in β Cu–Zn–Al were investigated between room temperature and 150 °C. Single crystal samples with surface normal close to $[001]_\beta$ were irradiated with 300 keV Cu^+ ions. Microstructural changes were characterized using transmission electron microscopy. Irradiation induced cavities located on the surface exposed to the irradiation were observed. The morphology, size and density distribution of these cavities were analyzed as a function of different irradiation conditions. The shape and location of the cavities with respect to the irradiation surface were not affected by irradiation temperature or irradiation dose. Instead, the cavity size distribution showed a bi-modal shape for a dose of 15 dpa, regardless of irradiation temperature. For a dose of 30 dpa the bi-modal distribution was only observed after room temperature irradiation. The diffusion effects of vacancies produced by irradiation are analyzed in shape memory Cu–Zn–Al alloys, which main characteristic is the diffusionless martensitic transformation. Particularly, the cavity size distributions were analyzed in terms of nucleation, growth and coalescence.

1. Introduction

Phase stability in Cu–Zn–Al alloys is related to the electron concentration or number of conduction electrons per atom (e/a). This system is well-known for its shape memory characteristics. It undergoes a reversible martensitic transformation from an $L2_1$ ordered high temperature cubic austenite (β) phase to a monoclinic martensitic structure, when the e/a is near 1.48 [1]. Since this transformation is diffusionless the atomic ordering in the product phase is inherited from the parent phase. Like in many other shape memory alloys, the martensitic transformation temperature between the austenite and martensite phases in Cu based systems depends strongly on composition [1], degree of long-range order [2] and the presence of structural defects, such as dislocations or second phase precipitates [1,3]. Therefore, diffusion processes that occur through the migration of vacancies may result in transformation temperature shifts. For example, annealing of quenched-in disorder in the β phase or precipitation of the γ phase modify the transformation temperature [3,4], in a similar way as local composition inhomogeneities in melt-spun Ni–Al [5] or Ti_2Ni or other precipitates in ternary Ti–Ni–X systems [6]. Moreover, systems like $Ti_{36}Ni_{49-x}Hf_{15}Cu_x$ ($x = 5$, 8) shows a dramatic decrease of the martensitic transformation temperature when the annealing one is higher than 873 K due to the coarsening of the $(Ti,Hf)_2Ni$ particles [7].

Also, since the atomic order inherited by the martensite phase is not the most stable configuration in this system, diffusional reordering processes in the martensite phase can take place when sufficient driving energy is provided, and result in a reduction of the Gibbs energy, leading to stabilization, which implies an increase of the retransformation temperature from the martensite to the austenite [8].

Irradiation can lead to microstructural changes such as disordering, radiation enhanced ordering or the precipitation of second phases [9]. Such effects in the austenite or martensite phases may influence the martensitic transformation temperature. Irradiation effects in Cu–Zn–Al alloys have been studied using neutrons, electrons and ions. The effects have been analyzed by either measuring the shifts in martensitic transformation temperature [10–13], or by characterization of the microstructural changes with transmission electron microscopy [14–18].

* Corresponding author. EMAT, University of Antwerp, Groenenborgerlaan 171, B-2020 Antwerp, Belgium. Tel.: +32 3 265 3331; fax: +32 3 265 32 57.
E-mail address: zelaya@cab.cnea.gov.ar (E. Zelaya).

0966-9795/$ – see front matter © 2009 Elsevier Ltd. All rights reserved.
doi:10.1016/j.intermet.2009.09.010

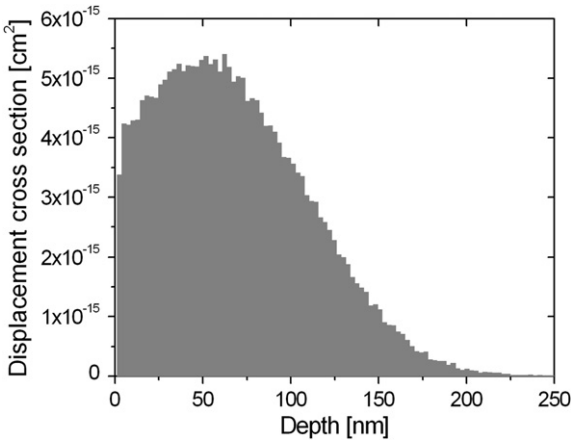

Fig. 1. Displacement cross-section as a function of depth for 300 keV Cu^+ ions in β Cu–Zn–Al calculated using SRIM code [23].

Low dose irradiation experiments in the austenite phase with electrons and neutrons have shown little effect on the martensitic transformation temperature, whereas large shifts were measured after irradiation in the martensite phase, due to irradiation induced stabilization [10,11,13]. In the austenite phase, dislocation loops were observed after neutron irradiation [12].

In order to study the effects of larger irradiation doses, ion irradiation experiments were carried out. For doses below about 5 displacements per atom (dpa) in the austenite at room temperature, changes in the degree of long-range order, the formation of close packed structures on the surface exposed to irradiation and the precipitation of the γ phase in the bulk were observed [14–16]. However, no such changes were observed if the irradiation was carried out at 300 °C [19]. In the martensite phase, small nanometer-sized defects were observed after low dose swift heavy ion irradiation [18].

In the austenite phase, the formation of cavities was first observed following 300 keV Cu^+ ion irradiation up to a dose of 30 dpa [20]. Cavities were found to have a large dispersion in size and were faceted parallel to the $\{001\}_\beta$ planes.

The aim of this work is to study irradiation induced cavities in the austenite β phase in Cu–Zn–Al in detail. For this purpose, high dose 300 keV Cu^+ ion irradiations are carried out, and the effects of irradiation temperature and dose on the cavity morphology, size density and distribution is analyzed.

2. Experimental

A Cu-22.7at%Zn-12.7at%Al alloy was prepared in an electric furnace using pure metals sealed in a quartz capsule. From this material, a single crystal was grown by the Bridgman technique and oriented by X-ray diffractometry using the Laue method. To avoid the formation of surface martensite, which is always present on surfaces close to $\{011\}_\beta$ or $\{111\}_\beta$, a surface orientation close to $\{001\}_\beta$ was selected [21,22]. Based on this choice, slices in the shape of an oval disc of 6 mm × 8 mm × 1 mm were cut perpendicular to the $[001]_\beta$ direction using a low speed diamond saw. One side of these slices was then mechanically ground and electropolished using only one jet from a TENUPOL double jet instrument. A 500 ml distilled water, 250 ml ethyl alcohol, 250 ml orthophosphoric acid, 50 ml propyl alcohol and 5 g urea solution was used as electrolyte at 12 V and 5 °C.

These samples were irradiated with 300 keV Cu^+ ions with a mean flux of $5\cdot10^{12}$ ions/cm^{2}s. The displacement cross-section was determined using the SRIM code [23]. Fig. 1 shows the displacement cross-section as a function of depth for 300 keV Cu^+ ions in β Cu–Zn–Al. Within the surface and a depth of ≈100 nm, the estimated median value of the displacement cross-section is $\approx 3\cdot10^{-15}$ cm^2, resulting in a displacement rate of $1\cdot10^{-2}$ dpa/s. At larger depths the cross-section decreases significantly. Hence, we can infer that atomic displacements occurring beyond a thickness of 100 nm have negligible effects on the microstructural evolution. The irradiations were performed at room temperature, 100 °C and 150 °C, up to fluences of 15 dpa and 30 dpa. Consequently, each atom of the sample received 15 (samples irradiated up to 15 dpa) or 30 (samples irradiated up to 30 dpa) times the necessary energy to be displaced from its equilibrium site throughout the irradiation experiment. All the samples were irradiated perpendicular to the electropolished surface using the HVEE 500 kV accelerator at the Institute of Physics UFRGS, Porto Alegre, Brazil. The irradiation temperatures reported correspond to the substrate temperature. The actual specimen temperature during irradiation was not measured. However, under similar irradiation conditions and in specimens with a diameter of 3 mm and 0.2 to 0.3 mm thickness, the stationary state temperature during room temperature irradiation reported in reference [14] was 43 °C. In the present experiments, the specimens have a larger mass and therefore a lower temperature increase induced by the ion flux is expected.

The irradiated surfaces were covered with a lacquer. From each sample, two discs with a diameter of 3 mm were cut using spark erosion, and then mechanically grinded from the non-irradiated side to a thickness of 0.2 mm. In order to perform plan-view transmission electron microscopy (TEM) observations, the samples were further thinned from the non-irradiated side to perforation using the TENUPOL device. At the end, the lacquer over the irradiated surface was removed in an acetone bath and the sample was rinsed in ethanol. Additional cross-section thin-foil samples, parallel to the irradiation direction, were prepared using a FIB/SEM Nova 200 FEI dual-beam system at EMAT at the University of Antwerp in Belgium. The TEM observations were carried out in a CM20 FEI instrument operating at 200 keV.

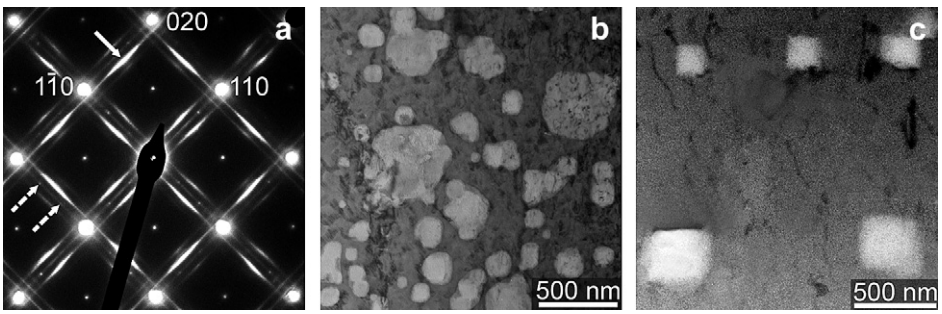

Fig. 2. (a) SAD pattern along the $[001]_\beta$ zone axis of an irradiated sample with 15 dpa at room temperature. Arrows indicate the extra spots due to phases precipitated during irradiation. (b) Bright field image corresponding to the SAD pattern shown in (a). (c) Bright field image of a sample irradiated up to 30 dpa at 150 °C.

The cavity number density was evaluated by analyzing at least 200 cavities in bright field images for each irradiation condition. The local thickness of the thin-foils was measured by comparing on-axis Convergent Beam Electron Diffraction (CBED) patterns with simulations based on the dynamical theory of diffraction [24]. The simulations were done using the cb3 program in the EMS software package [25]. This program is based on the Bloch wave formalism with electron scattering factors from Doyle and Turner [26]. The simulations were performed assuming the austenite B2 ordered structure of the Cu-22.7%atZn-12.7%atAl matrix, considering up to 69 reflections from the zero order Laue zone. The use of a $L2_1$ as unit cell yields the same results.

3. Results

The irradiated samples present a mixed microstructure with square shaped cavities and particles with a close packed crystal structure formed on the irradiated surface. Fig. 2a shows a selected area diffraction (SAD) pattern presenting characteristic diffraction spots of irradiated specimens [15,17]. Additional reflections are indicated with arrows on streaks parallel to the $[110]_\beta$ matrix direction, the full arrow indicating a 2H phase reflection while the dashed arrows indicate γ phase reflections. Fig. 2b and c show bright field images from samples irradiated to 15 dpa at room temperature (fig. 2b) and to 30 dpa at 150 °C (fig.2c). Both micrographs present cavities with faces roughly perpendicular to the $[100]_\beta$ and $[010]_\beta$ directions. Cavities with very heterogeneous sizes can be observed in fig. 2b. The boundaries of the cavities are not well defined due to the presence of a large amount of close packed phase particles covering the irradiated surface. The 30 dpa 150 °C irradiated sample presents a lower density of cavities but with a more homogeneous size and shape distribution (fig.2c). The close packed phase was not so abundant on the samples irradiated to a higher dose and at higher temperatures, so the cavity boundaries are better defined in fig.2c. The evolution of cavity size distribution and density as a function of irradiation dose and temperature is illustrated in fig. 3 and Table 1. Further analysis of the formation of both close packed phase and γ phase precipitation during irradiation will be presented in a forthcoming publication.

Fig. 3 a shows the size distribution of cavities in the $[100]_\beta$ direction for a 30 dpa room temperature irradiated sample. A single and a double peak Lorentz function are fitted to the distribution. In this case, it can be appreciated that the experimental distribution is better described by the bi-modal function. This curve shows a smaller χ^2 value than the simple Lorentz function (7.7 versus 9.9, resp.). χ^2 stands for the closeness of the values to the fit curve.

Taking into account this criterion, a single or a double peak Lorentz curve was fitted to each size distribution of every different irradiation condition. Fig. 3b and c show the best fitting curves for each histogram for the samples irradiated up to 15 dpa and 30 dpa, respectively. The 15 dpa samples show a bi-modal distribution for all irradiation temperatures. This behavior is more noticeable for the higher irradiation temperatures. Nevertheless, for the room temperature irradiation, a peak at 50 nm and another one at 100 nm can still be discriminated. The 30 dpa samples show a bi-modal distribution only for the room temperature irradiation.

In the room temperature irradiation experiments, a bi-modal size distribution is observed both at 15 dpa and 30 dpa, while the cavity density, i.e. the number of cavities per surface area, is found to increase with irradiation dose. Instead, in the irradiation experiments at 100 °C and 150 °C, the size distributions evolved form a bi-modal distribution at 15 dpa to a single peak distribution at 30 dpa. At the same time the cavity density dropped about 1 order of magnitude (Table 1).

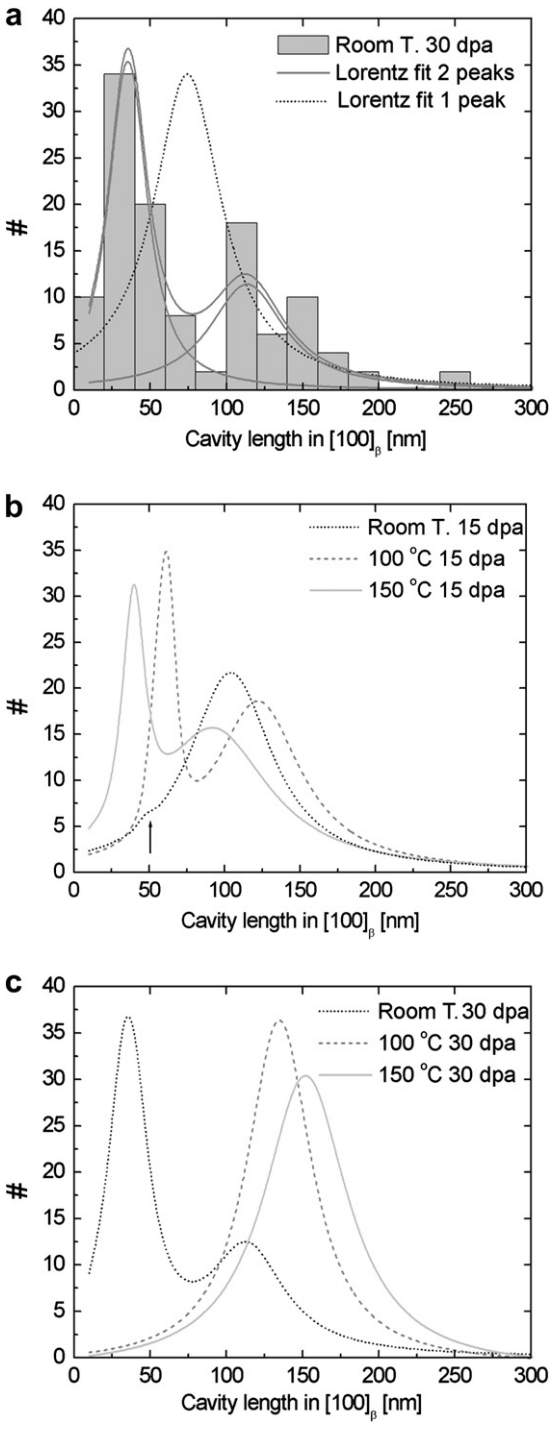

Fig. 3. Histograms of the size distribution of cavities observed along $[001]_\beta$ direction. (a) Size distribution observed after 30 dpa irradiation dose at room temperature. Two peaks and one peak Lorentz curves are fitted to the histogram. (b) Best fit-curves for each distribution, at room temperature, 100 °C and 150 °C for irradiation up to 15 dpa. The arrow indicates the first Lorentz peak of the distribution obtained at room temperature. (c) Best fit-curves for each distribution, at room temperature, 100 °C and 150 °C for irradiation up to 30 dpa.

In order to test for possible projection errors in the TEM micrographs, the lateral dimensions (x, y axis) as well as their sizes along the depth direction (z axis) of some individual cavities were determined experimentally. The z sizes were inferred for the difference between the local thicknesses at a cavity site and that in the crystal matrix surrounding the cavity. Local thicknesses were

Table 1
Cavity density per unit area and mean cavity size for each irradiation condition. Room T. refers to room temperature.

Irradiation condition	Cavity density per unit area [cm^{-2}]	Mean cavity size along $[100]_\beta$ [nm]		
		One peak	Two peaks	
Room T. 15 dpa	$(11 \pm 1)\cdot 10^8$	–	50 ± 2	100 ± 60
100 °C 15 dpa	$(10 \pm 5)\cdot 10^8$	–	60 ± 9	120 ± 60
150 °C 15 dpa	$(8 \pm 2)\cdot 10^8$	–	40 ± 10	90 ± 80
Room T. 30 dpa	$(18 \pm 3)\cdot 10^8$	–	40 ± 30	110 ± 60
100 °C 30 dpa	$(0.6 \pm 0.2)\cdot 10^8$	130 ± 50	–	–
150 °C 30 dpa	$(1.2 \pm 0.2)\cdot 10^8$	150 ± 60	–	–

measured by comparing experimental $[001]_\beta$ zone axes CBED patterns with simulated patterns. Fig. 4 shows the comparison between the experimental CBED patterns and the corresponding and matching simulated ones. All the analyzed cavities present a depth (d) smaller than their lateral length (l) measured along the $[100]_\beta$ and $[010]_\beta$ directions. The aspect ratios (l/d) of the cavities vary between 10 and 3 independent of the irradiation conditions. This method is useful to determine the dimension of the cavities, but their location inside the matrix could not be deduced in this way. For this reason, FIB cuts were prepared for the 15 and 30 dpa irradiated samples at 100 °C. In all lamellae, the cavities were found to be located next to the irradiated surface. Fig. 5 shows a cavity covered by the Pt layer used to protect the area of interest of the sample during FIB thinning. The aspect ratio of this particular example is 4, confirming the above CBED conclusion. The localization of the cavities at the irradiated surface and the measured depths parallel to the $[001]_\beta$ direction (d), that were shorter than the implantation range (100 nm), imply that the above listed variations in cavity density are not due to an image projection effect.

4. Discussion

The present results show the formation of cavities located on the irradiated surface of a single crystalline β phase Cu–Zn–Al alloy, after irradiation with 300 keV Cu^+ ions in the temperature range between room temperature and 150 °C. The cavities were found to be shallow, that is, their depth was between 0.1 and 0.3 of their sides' length. Irradiation induced cavities in this system were reported previously after 300 keV Cu^+ ion irradiation [20], and after swift heavy ion irradiation [17]. In this work it was shown that the cavities are located on the surface exposed to irradiation. In all cases, the projected shape of the cavities was square with the principle facets parallel to the $\{100\}_\beta$ planes. The present results show that this morphology is independent of irradiation temperature within the range studied (homologous temperature (T_h) between 0.24 and 0.33). Still, the {100} facets do not correspond to the planes with lowest surface energy. As discussed in reference [27], {100} facets have been reported in voids induced by neutron irradiation in Mo at 760 °C ($T_h = 0.35$). However, in the same material voids with large {110} facets truncated by {001} facets were reported at a higher neutron irradiation temperature (1000 °C, $T_h = 0.44$). This suggests that cavities with {110} facets could be expected at higher irradiation temperatures. However, such experiments cannot be carried out in β Cu–Zn–Al due to decomposition into equilibrium phases.

In order to get more insight into the mechanisms controlling the formation of the void systems we have estimated their total vacancy content. In the following, the 15 dpa dose experiment at room temperature is analyzed in more detail. As mentioned above, the depth of the cavities in the $[001]_\beta$ direction is at least 3 times smaller than in the lateral $[100]_\beta$ and $[010]_\beta$ directions. The mean width of the cavities in a sample irradiated up to 15 dpa at room temperature in the $[100]_\beta$ direction is 100 nm (Table 1). So, an average cavity under this irradiation condition has a volume of 3 10^5 nm^3. Considering a lattice parameter of 0.2935 nm for a B2 unit cell with two atoms [28] an average sized cavity consumes $n_v = 2$ 10^7 vacancies. The total number of vacancies (N) in each cm^3 or density of vacancies due to the presence of cavities is given by:

$$N = n_v \times D = 2\cdot 10^7 \times 9\cdot 10^{13}\,cm^{-3} = 2\cdot 10^{21}\,cm^{-3} \quad (1)$$

where D stands for the density of cavities per unit volume measured for this irradiation temperature condition. Since the cavity density values were measured over a surface area larger than $3\cdot 10^{-7}$ cm^2, a rough estimate of the cavity density per unit volume can be calculated. Indeed, again using CBED to determine the mean thickness of the mentioned area, a $9\cdot 10^{13}$ cm^{-3} volume density was calculated for this sample. Taking into account that each cm^3 has $8\cdot 10^{22}$atoms, the volume fraction of vacancies contained in the cavities is 0.025. This value is several orders of magnitude smaller than the total displacements produced by irradiation for a 15 dpa dose (15 vacancies per atom). The volume fraction is also much smaller than the fraction of freely-migrating vacancies, which is usually a few percent of the vacancies produced [29]. Since no cavities were observed within the bulk of the specimens, this indicates that most of the freely-migrating vacancies are annihilated at the specimen surface.

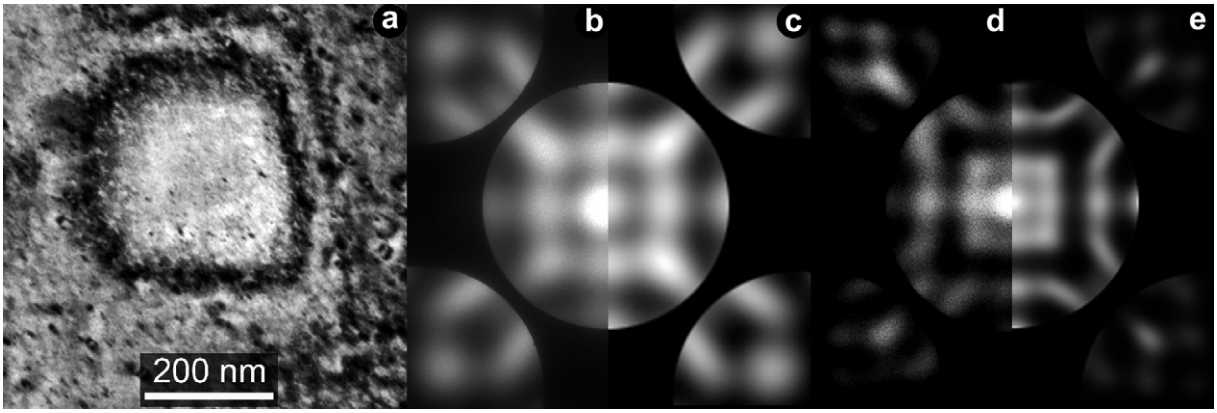

Fig. 4. (a) Bright field image in two beam condition of a cavity of (300 ± 10) nm measured along $[100]_\beta$ direction. (b) Left half of CBED performed inside the cavity. (c) Simulation of right half of CBED pattern of a 82 nm thick foil. (d) Left half of CBED performed next to the cavity. (e) Simulation of right half of CBED pattern of a 120 nm thick foil.

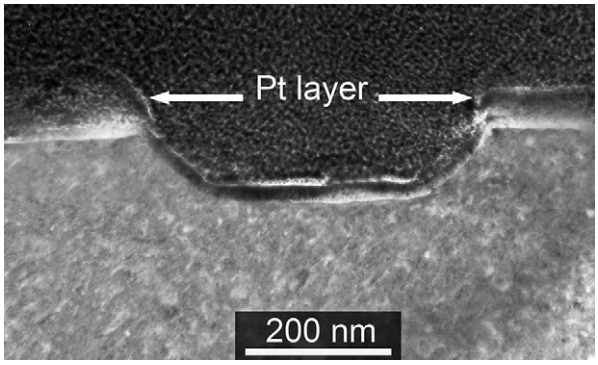

Fig. 5. Bright field image of cross-section prepared using FIB sectioning from the surface of a sample irradiated up to 15 dpa at 100 °C. A cavity next to the irradiated surface (covered with platinum) can be observed.

The observed cavity formation at room temperature is related to the low migration energy of vacancies. In β Cu–Zn–Al, the vacancy migration energy was found to be between 0.62 and 0.65 eV from positron annihilation experiments [30]. Values as low as these ones account for high vacancy mobility at room temperature, which is required for cavity formation.

The cavity size distribution is found to be bi-modal for room temperature irradiations while at 100 °C and 150 °C the distribution changes from bi-modal to single-peaked between 15 dpa and 30 dpa. Bi-modal size distributions have been found to result from nucleation and coalescence processes occurring concurrently [31]. Following this interpretation, the smaller sized cavities result from nucleation, while the larger sized cavities result from coalescence processes.

During irradiation vacancies are created at a constant rate and the main annihilation process occurs at the specimen surface. Considering that the sink strength of the surface is constant during irradiation, a stationary vacancy concentration is expected. The nucleation peak can therefore be explained by the supersaturation of vacancies, which provides a driving force for nucleation of cavities throughout the entire irradiation process.

The larger sized cavities are explained by coalescence processes that require cavity mobility in order to take place. Calculations performed in steel reveal that void coalescence provides an important channel for consolidation of vacancy defects into large and stable voids [32].

The cavity distributions at 100 °C and 150 °C were found to evolve from a bi-modal distribution to a distribution with a single peak corresponding to the large sized cavities of the former bi-modal distribution. This behavior suggests that nucleation processes are less effective at high doses at the higher irradiation temperatures, while coalescence processes continue to be active. As the irradiation temperature increases, vacancy mobility increases, and causes the stationary state vacancy concentration to decrease. Thus a smaller driving force for cavity nucleation would be expected as irradiation temperature increases. On the other hand, higher vacancy mobility favors cavity migration, and consequently facilitates cavity coalescence. Therefore, increasing irradiation temperature favors a single-peaked size distribution. However, the evolution from bi-modal size distribution into a single-peaked distribution cannot be accounted for by higher vacancy mobility alone. Further experiments and simulations are needed to clarify this point.

5. Conclusions

A single crystal β Cu–Zn–Al shape memory alloy with surface normal close to $[001]_\beta$ was irradiated with high doses of 300 keV Cu^+ ions between room temperature and 150 °C. Cavities located on the irradiated surface were observed and characterized. The shape of the cavities is not affected by the temperature. The size distribution of irradiation induced cavities reveals a bi-modal shape for room temperature irradiations. At 100 °C and 150 °C the size distribution evolves from bi-modal for a fluence of 15 dpa to single-peaked for a dose of 30 dpa. This behavior can be explained by a reduced driving force for nucleation and enhanced cavity migration at higher irradiation temperatures that can partially be accounted for by the higher vacancy mobility.

Acknowledgements

IAEA is acknowledged for financial assistance for E. Zelaya. This research work was performed with the support of a research project of the National Science Foundation of Flanders entitled "Optimization of Focused Ion Beam (FIB) sample preparation for transmission electron microscopy of alloys" (G.0180.08).

References

[1] Ahlers M. Martensite and equilibrium phases in Cu–Zn and Cu–Zn–Al alloys. Prog Mater Sci. 1986;30:135–86.
[2] Lanzini F, Romero R, Castro ML. Influence of Be addition on order–disorder transformations in β Cu–Al. Intermetallics 2008;16:1090–4.
[3] Cuniberti A, Montecinos S, Lovey FC. Effect of γ_2-phase precipitates on the martensitic transformation of a β-CuAlBe shape memory alloy. Intermetallics 2009;17:435–40.
[4] Rapacioli R, Ahlers M. The influence of short-range disorder on te martensitic transformation in Cu–Zn and Cu–Zn–Al alloys. Acta Metall 1979;27:777–84.
[5] Potapov PL, Ochin P, Pons J, Schryvers D. Nanoscale inhomogeneities in melt spun Ni–Al. Acta Metall 2000;48:3833–45.
[6] Delville R, Schryvers D, Zhang Z, James RD. Transmission electron microscopy investigation of microstructures in low-hysteresis alloys with special lattice parameters. Scr Mater 2009;60:293–6.
[7] Meng XL, Cai W, Fu YD, Li QF, Zhang JX, Zhao LC. Shape-memory behaviors in an aged Ni-rich TiNiHf high temperature shape-memory alloy. Intermetallics 2008;16:698–705.
[8] Abu Arab A, Ahlers M. The stabilization of martensite in Cu–Zn–Al alloys. Acta Metall 1988;36:2627–38.
[9] Wollenberger H. Phase transformations under irradiation. J Nucl Mater 1994;216:63–77.
[10] Tolley A, Ahlers M. Influence of neutron irradiation on the martensitic transformation in 18R Cu–Zn–Al single crystals. Scr Metall 1989;23:2117–20.
[11] Tolley A. The effect of electron irradiation on the ß/18R martensitic transformation in CuZnAl alloys. Radiat Eff Defects Solids 1994;128:229–45.
[12] Tolley A. The effect of low dose neutron irradiation in Cu–Zn–Al shape memory alloys. Z Metallkd 1994;85:877–9.
[13] Tolley A, Macht MP, Müller M, Abromeit C, Wollenberger H. The stabilisation of Cu–Zn–Al 18R martensite by 2 MeV proton irradiation. Philos Mag 1995;72A:1633–47.
[14] Tolley A, Abromeit C. Microstructural changes due to ion irradiation in ß-CuZnAl alloys. Scr Metall Mater 1995;32:925–30.
[15] Zelaya E, Tolley A, Condó AM, Lovey FC, Fichtner PFP, Bozzano P. Ion irradiation induced formation of close packed particles in Cu–Zn–Al. Scr Mater 2005;53:109–14.
[16] Zelaya E, Tolley A, Condó AM, Lovey FC, Fichtner PFP. Ion irradiation induced precipitation of γ phase in Cu–Zn–Al–Ni. Mater Sci Eng A 2007;444:178–83.
[17] Zelaya E, Tolley A, Schumacher G. Microstructural changes in β–Cu–Zn–Al due to SHI irradiation. Nucl Instrum Methods B 2009;267:63–8.
[18] Zelaya E, Tolley A, Condo AM, Schumacher G. Swift heavy ion irradiation of Cu–Zn–Al and Cu–Al–Ni alloys. J Phys: Condens Matter 2009;21:185009 (8pp).
[19] A. Tolley and C. Abromeit, unpublished results.
[20] E. Zelaya "Stability of phases under irradiation on Cu based alloys", PhD Thesis IB-UNC; 2006.
[21] Lovey FC, Chandrasekaran M, Rapacioli R, Ahlers M. Diffraction effects in β-Cu–Zn–Al. Observation and interpretation of extra maxima. Z Metallkd 1980:37–41.
[22] Lovey FC, van Tendeloo G, van Landuyt J, Chandrasekaran M, Amelinckx M. The origin of the incommensurate electron diffraction patterns in γ-brass type precipitates in β Cu–Zn–Al alloy. Scr Acta Metall 1984:879–86.
[23] Biersack JP, Haggmark LG. A Monte Carlo computer program for the transport of energetic ions in amorphous targets. Nucl Instrum Methods 1980;174:257–69.
[24] Castro Riglos MV, Tolley A. A method for thin foil thickness determination by transmission electron microscopy. Appl Surf Sci 2007;254:420–4.
[25] Stadelmann PA. EMS - A share package for electron diffraction analysis and HREM image simulation in materials science. Ultramicroscopy 1987;vol 21:131–45.
[26] Doyle PA, Turner PS. Relativistic Hartree-Fock X-ray and Electron Scattering Factors. Acta Crystallogr 1968;A24:390–7.

[27] Rau RC, Secco F, Aragona Ď, Ladd RL. Neutron damage in molybdenum irradiated at high temperatures. Phil Mag 1970;21:441–52.
[28] Lee IC, Chung IS. The origin of reverse shape memory effect in a Cu–Zn–Al alloy. Scr Metall 1989;23(I2):161–6.
[29] Zinkle SJ, Singh BN. Defect accumulation in pure fcc metals in the transient regime: a review. J Nucl Mater 1993;199:173–91.
[30] Romero R, Somoza A. Point defects behavior in beta Cu-based shape memory alloys. Mater Sci Eng A 1999;273–275:572–6.
[31] Preininger D, Kaletta D. The growth of gas-bubbles by coalescence in solids during continuous gas generation. J Nucl Mater 1983;117:239–43.
[32] Surh MP, Sturgeon JB, Wolfer WG. Void nucleation, growth, and coalescence in irradiated metals. J Nucl Mater 2008;378:86–97.